ADVANCED ENGINEERING MATERIALS
www.aem-journal.com

# High-Throughput Micromechanical Testing Enabled by Optimized Direct Laser Writing

*Alexander Jelinek,* Stanislav Zak, Markus Alfreider, and Daniel Kiener*

**Direct laser writing by two-photon lithography enables the manufacturing of tailored 3D objects, commonly referred to as 3D-printing, with submicrometer precision. Thereby, new approaches are enabled for miniaturized optical and mechanical devices, where basic material properties act as design guideline and initial input for finite element simulation-driven device design. These mechanical properties are accessible through micromechanical testing and suitably adapted miniaturized specimens. With direct laser writing, a micromechanical specimen geometry can be readily manufactured without additional postprocessing, enabling the possibility of repetitive sample production and further high-throughput testing. Widely overhanging features, as in common bending beam or tension specimens, easily cause floating layers as writing artifacts and thereby undefined geometries. Within this work, an approach to overcome this issue is presented. By introducing a slight taper within the geometry at initially printed layers, a reliable sample geometry is achievable without changing the overall mechanical behavior. As showcase geometries, miniaturized notched cantilever and advanced push-to-pull devices incorporating a notched tension specimen are detailed. Mechanical testing is conducted in situ and ex situ, and the mechanical influence from introducing a taper to a straight geometry is assessed via a finite element modeling. Thereby, a comprehensive approach for high-throughput micromechanical testing is established.**

## 1. Introduction

With increasing application of direct laser writing in various research fields, the mechanical characterization of cured polymer structures is essential. Besides common elastic properties such as Young's modulus and Poisson's ratio, also failure characteristics like the yield strength or fracture toughness are required as basic design criteria for mechanically loaded structures.[1,2] Due to the inherent structure of cured polymers, they exhibit viscoelastic, temperature, and loading rate dependent characteristics, which are majorly influenced by the actual curing process parameters and the storage history.[3,4] Postcuring by heating or UV irradiation allows some influencing parameters to be homogenized, although side effects such as shrinkage will always evolve.[5–7] Another approach to chemically transfer the cross-linked polymer is carbonization via a heat treatment to obtain glassy carbon, offering a higher strength at the downside of an increased brittle character.[8–11]

Investigating the mechanical properties of direct laser-written structures, which are components of micro-/nanomechanical devices, needs to be conducted in the native scale of such devices due to effects of very confined polymerized volumes. Hereby, various methods reaching from nanoindentation, pillar compression, micro beam bending, and micro notched tension experiments can be applied.[4] The free-form ability and precise control regarding specimen shape is thereby of great advantage. If side effects such as shrinkage are accounted, a well-defined specimen geometry is generated without the need for postapplication of localized processing via, e.g., ion slicing or focused ion beam milling.[5,11,12] In essence, no side effects on sample preparation are present and only material and processing properties determine the experimental results. But the far most advantage in terms of materials testing is that every printed geometry originates from the same digital model and will thereby possess the exact same dimensions within the tolerances of the manufacturing process. This fact, in conjunction with reasonable and automated sample fabrication, enables high-throughput sample testing and allows to achieve statistical valid material properties or precisely study influences of individual parameters with low effort compared to other micrometer scale processing techniques, at least for available photoresist materials.

Fundamental experiments as such will be helpful for future applications because direct laser writing enables new technological approaches, for example, in optics,[13–16] photonics,[17] medicine,[18,19] microfluidics,[20,21] and microrobotics.[22,23] Although the broad practical application is only in the early stages, commercial devices are already available, capable of processing waver size substrates, and thereby driving the

A. Jelinek, M. Alfreider, D. Kiener
Department of Materials Science
Montanuniversität Leoben
Franz-Josef-Straße 18, 8700 Leoben, Austria
E-mail: alexander.jelinek@unileoben.ac.at

S. Zak
Erich Schmid Institute for Materials Science
Austrian Academy of Sciences
Jahnstraße 12, 8700 Leoben, Austria

The ORCID identification number(s) for the author(s) of this article can be found under https://doi.org/10.1002/adem.202200288.



**DOI: 10.1002/adem.202200288**

development toward integration within conventional small-scale fabrication facilities as used in the semiconducting industry.

Representatively considering the consumer electronics sector, it is evident that future applications will be employed in various environmental conditions, such as elevated temperatures due to sun irradiation or various humidity levels, also including long-time exposure to them.[24] Thus, mechanical testing under various environmental influences will be a perspective to increase durability and reliability of direct laser-written components. For devices under application conditions, failure by mechanical fracture could arise from thermal mismatch, shock loading, or aging of polymeric components. Thus, micromechanical fracture experiments should be performed to study a large variety of environmental influences and loading conditions on miniaturized specimen geometries or reprinted operational application parts. However, fracture mechanical experiments commonly suffer from certain scatter due to various experimental influences. Here, the high-throughput aspect on sample testing will be additionally beneficial to increase the precision of material and environmental material influence characterization.

However, before a broad range of materials parameter testing can be achieved, shortcomings of the sample preparation process must be accounted for, to take advantage of direct laser-written specimen geometries. Besides common adhesion issues on the substrate and material shrinkage, which can be systematically accounted for, large overhanging features seem to be the most prominent source for uncontrolled geometry deviations, due to inadequate cohesion between the first few printed layers over long distances. Therefore, this work aims for an optimization approach to account for this issue and thereby establish the possibility to perform high-throughput sample testing and limit the experimental scatter according to such undefined geometries. Remaining sources of experimental scatter are noise in the force, measurement errors of testing dimensions, as they are always present in mechanical experiments. Furthermore, also discretization errors are present, given the geometries are small such that individual features, e.g., notches or edges, are near the resolution limit of the device. However, as they are reproducible a consistent geometry along all specimens is ensured, which is very helpful for many individual experiments, as the time-consuming determination of each individual specimen dimension can be skipped. The focus is placed on miniaturized fracture experiments via notched bending beam specimens and an advanced push-to-pull (PTP) device geometry incorporating a double edge notched tension (DENT) specimen.[25] Generally, the resulting methodology is generic and easily applicable for other printed designs.

## 2. Results and Discussion

The two chosen fracture mechanical specimen geometries constructed for the manufacturing via direct laser writing are shown in **Figure 1**a,b. Figure 1a is a rendered image of a notched bending beam with common aspect ratio, attached to a pyramidal base block with sufficient height and adhesion area to ensure a fixed position during conduction of the mechanical experiment. Figure 1b depicts a PTP geometry, intended to conduct tension experiments by applying experimentally less demanding compressive loading. The upper block is equipped with a rounded top to establish a reliable contact, even if small misalignments are present. For an optimal case, a flat-punch-shaped indenter tip is used. The upper and lower blocks are connected via two arms that transform the compressive load to tension by bending outward during loading. In between, a sample geometry can be inserted, which is in this case a DENT shape. However, as this part is the geometrically weakest spot, alternative shapes are also possible. Further design details regarding the geometries can be found in the experimental section. First printing attempts (refer to scanning electron microscope (SEM) images in Figure 1c,d) of these specimen types depicted considerable printing artifacts at highly overhanging positions. The splitting of the geometry to a lamella like shape is caused by the drifting motion of fragile initially printed layers within the fluid resin, as no second anchoring point is present far from the base. After a certain number of written layers this loose structure supports subsequently printed ones, thus finally forming a bulky geometry on top. Although this artifact presumably has only a minor mechanical influence on the notched regions, the experimental loading results can be influenced by a premature touch down at higher bending displacements. For the case of the notched tension samples, the nonuniform shape deviation will also introduce geometrical errors along the printed versions, affecting in particular the bottom notch geometry.

For a repetitive and reproducible specimen fabrication, a systematic approach to avoid these kinds of artifacts is necessary. An optimized writing strategy and certain parameters could potentially reduce the extend of these, although none are documented to the authors' knowledge for overhanging features which exceed 100 µm, as shown in Figure 1a,c, and avoid block-wise splitting of the structure in a liquid resin formulation. Therefore, a slight change in geometry might solve this issue in any case and without altering the standard print-preparation procedure. Massive supporting structures would be one way to avoid the motion of initially printed structures. These additional structures must be removed in a separate milling step to achieve a free-standing specimen, which would counteract high-throughput attempts. As low aspect ratio overhanging features pose no issue, another approach is to reduce the individual overhanging distance of consecutively printed layers. Thereby, previous layers act as sufficiently solid base for the following ones, as indicated in **Figure 2**a. This is practically realized by introducing a small taper on faces pointing toward the substrate surface. Figure 2b illustrates a sidewise projection of the original notched cantilever shape, while in Figure 2c an adopted version including a 2° taper is introduced. In analogy, tapers are introduced on the notched tension specimen within the PTP device, in this case on the top and bottom side to preserve symmetry (see Figure 2d,e**)**. The drawback of this method is that a geometrical deviation from a standard uniform geometry could influence the overall mechanical behavior, which should then be accounted for in the evaluation. In detail, the reduced thickness of the notched cantilever ligament results in a decreased response force and the nonuniform beam cross section in a deviation from the ideal deflection curve. For the case of the tension specimen, a more uniform loading is present to which small changes will cause only minor effects. However, the magnitude of geometrical

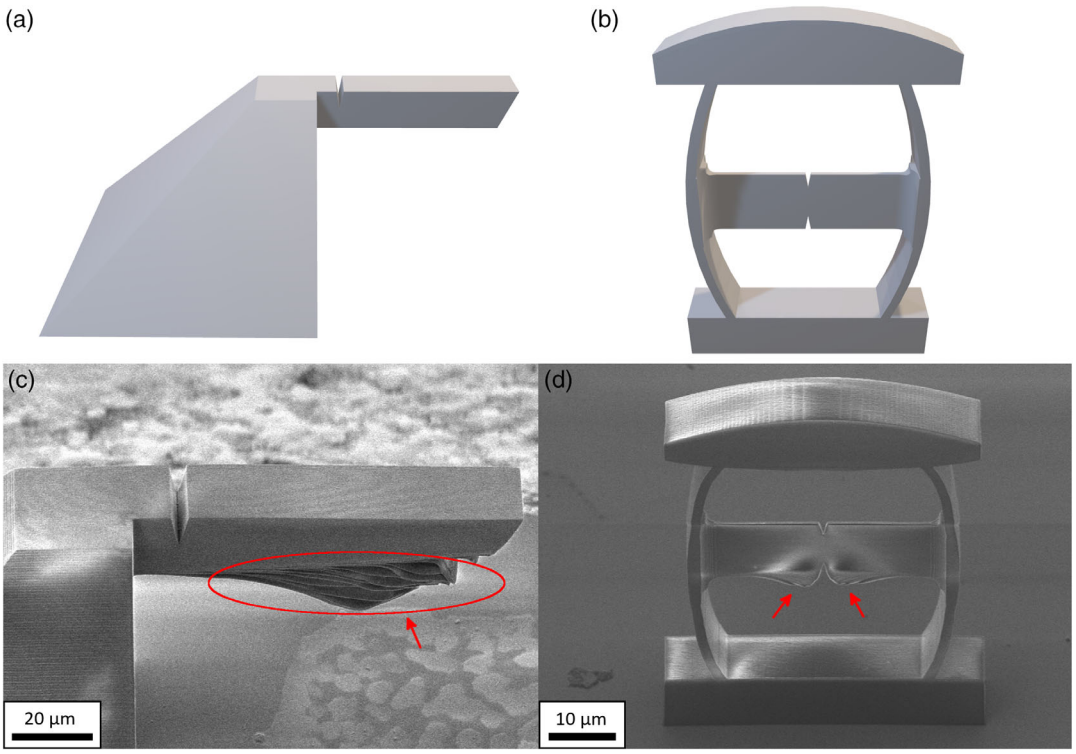


**Figure 1.** Miniaturized mechanical fracture specimen geometries, designed for direct laser writing of a) notched cantilevers and b) PTP devices incorporating a DENT specimen region. c) Resulting notched cantilever geometry with printing artifacts due to large overhanging distance. d) PTP device after direct laser writing. Note printing artifacts near the bottom notched region indicated via arrows.


**Figure 2.** a) Printing strategy to overcome printing artifacts for large overhanging distances, with tapered geometry on faces pointing downward. Dark and light gray area indicates printed structure and layers. In red, printing from bottom to top with voxel and beam path for two-photon polymerization is indicated. Thereby, the overhanging distance at initially printed layers is reduced, decreasing the tendency of floating out of place before subsequent layers are cured. b) Side view of ideal notched cantilever and under c) a version prepared with the printing strategy depicted in (a), with changes (dashed line) aiming for a precisely defined physical specimen. For the double notched tension geometry in d), the same approach is applied in e) on the upper and lower side to preserve the symmetry.

errors due to the tapered geometry changes will be discussed later based on finite element (FE) analysis.

In **Figure 3**a, a tapered notched cantilever geometry is shown, while Figure 3b depicts a magnified SEM image of the cantilever tip, without major printing artifacts discernible. Step shaped layers on the bottom edge represent the physical representation of the principle indicated in Figure 2a. A minor drifting effect remained, already diminishing at the second consecutively printed layer. Multiple uniformly shaped specimens can be conveniently printed on a suitably prepared substrate, giving a sample array as indicated in Figure 3c, ready for subsequent in situ SEM testing. For the case of PTP devices, a pure adoption of the taper did not resolve all printing artifacts at the first print of the optimized geometry right away. Residual printing artifacts still appeared at the overhanging feature near the notch. Presumably initially printed lines were not stable enough for the case of low specimen thickness of just a few voxels diameter. However, after a slight increase of writing power, fully stable

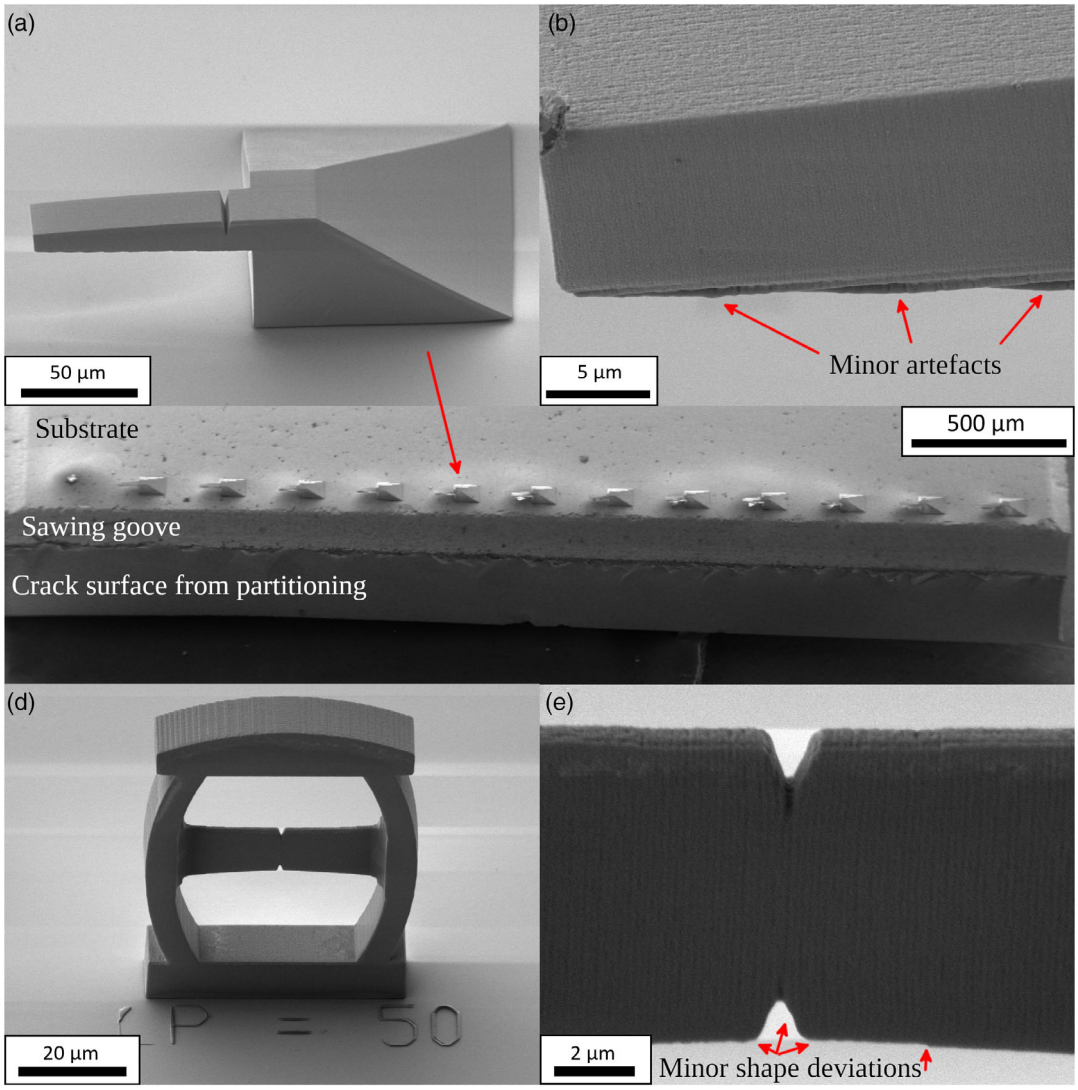


**Figure 3.** a) Optimized notched cantilever geometry fabricated via direct laser writing without printing artifacts. b) Magnified detail of the cantilever tip. Large printing artifacts are absent, just minor features remained. c) Twelve notched cantilever specimens printed side by side on a preprepared substrate demonstrating the high-throughput testing possibility. d) Optimized PTP DENT specimen, printed with slightly increased laser writing power without any printing artifacts visible. e) Higher magnification detail of the notched region, with just minor deviations from the ideal shape at the resolution limit of the printing device.

prints were obtained as indicated in Figure 3d, exhibiting well-defined notched regions shown in detail in Figure 3e. Residual minor specimen shape imperfections originate from printing at the resolution limit of the employed printing device. Furthermore, the thickness of the bending arms was increased to heighten the overall stability before conducting the actual fracture experiments.

Equivalent digital models can be employed for FE analysis as for direct laser writing. For a direct comparison, the actual taper after the development procedure of the specimen must be considered, which is about 4.4° for the case of the cantilever and 3.5° for the PTP specimen in the present case. Presumably these values will vary to a certain extent, along different geometries and laser writing parameters used. However, here the focus was placed on the direct comparison between nontapered and tapered versions, in the sense that a comparison was done both qualitatively (in terms of the overall stress distribution) and quantitatively (in terms of the geometry/calibration functions). The linear-elastic simulations were carried out using previously determined material parameters and are comparable to the conducted mechanical experiments.[4] **Figure 4** shows a comprehensive overview of the simulation results. In Figure 4a,b, the von-Mises equivalent stress field around the notch is shown for the nontapered and tapered version of the notched cantilever specimen geometry, respectively. The stress fields appear qualitatively similar, but a slightly higher overall stress is present for the tapered geometry due to a smaller ligament size. Concerning the PTP devices incorporating tension specimens in Figure 4c,d,

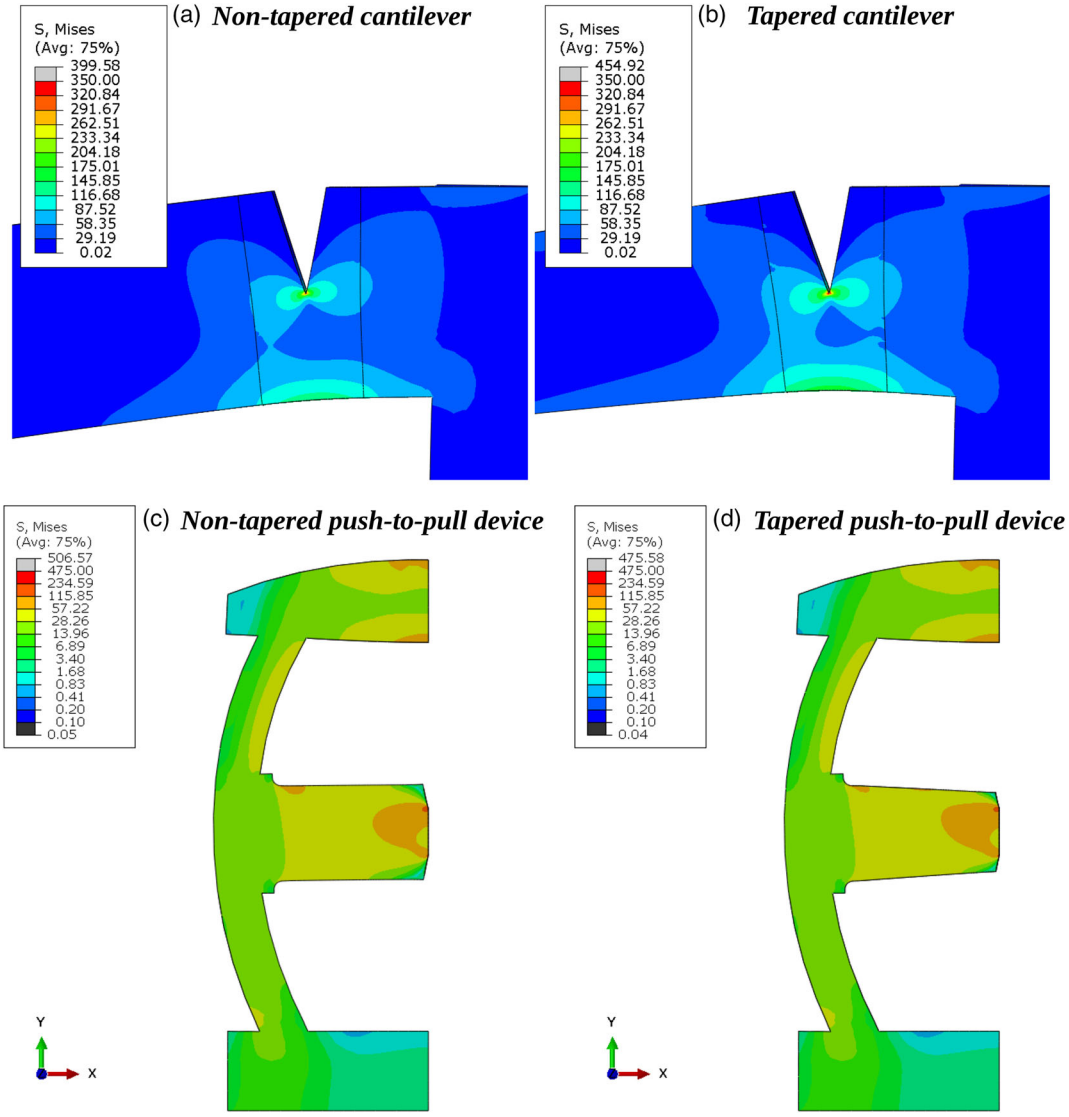


**Figure 4.** Linear elastic 3D FE analysis of the von-Mises stress distribution within the cantilever showing a) constant cross section of 20 × 20 µm and b) including 4.4° taper, loaded at 60 µm from the notch. Equivalent simulation results are shown in (c) for nontapered and d) for tapered realizations of the PTP device including 3.5° taper.

a central-symmetrical model was employed and the von-Mises equivalent stress map is shown. Here also just a minor overall increase of stress within the tapered tension specimen is present due to the decreasing specimen cross section toward the notch. Furthermore, the images reveal no other explicit critical stress concentrations besides the notch. At this point it must be emphasized that no viscoelastic or plastic processes are considered. Nevertheless, a quick assessment revealed that the introduction of a comparably small taper seems to just slightly influence the overall mechanical behavior and will therefore not influence mechanical experiments to a significant extent.

To quantify the impact of the tapered geometry on the resulting fracture properties, geometry functions for the cantilever and PTP device were derived for tapered and nontapered versions. Resulting mode I stress intensity factor $K_I$ values extracted from the FE models were processed in terms of standard $K_I$ to stress and geometry relation as shown by Equation (1).[26]

$$K_I = Y\left(\frac{a}{W}\right)\sigma\sqrt{\pi a} \tag{1}$$

where $\sigma$ is the nominal stress in the specimen, $a$ is the crack length, $W$ is the full specimen width, and $Y(a/W)$ is the calibration function, respectively. In case of the PTP device, the formula can be rewritten in the form of Equation (2), where $b$ is the remaining ligament thickness, $F$ is the loading force of the indenter on the top of the sample, and $W$ is the full width of the tested section for both tapered and nontapered model (neglecting the taper).

$$Y_{\mathrm{PTP}}\left(\frac{a}{W}\right) = \frac{K_I \cdot b \cdot W}{F \cdot \sqrt{\pi a}} \tag{2}$$

This can be used with the assumption that the taper only acts as a "wide notch" on top of the specimen, not reducing the ligament length.

However, in case of the cantilever, the taper decreases the ligament length, regardless of the crack length. Therefore, the specimen width at the exact crack position $W^*$, taking the taper into account, must be defined for calibration. With it, the calibration function can be defined as indicated by Equation (3), where $L$ is the distance from the loading point to the crack plane.[27]

$$Y_{\mathrm{Cantilever}}\left(\frac{a}{W^*}\right) = \frac{K_I \cdot b \cdot W^{*2}}{6 \cdot F \cdot L \cdot \sqrt{\pi a}} \tag{3}$$

With these $Y$-functions defined and calculated for a wide range of crack lengths, both specimen types show negligible differences in terms of the fracture mechanical behavior, as indicated in **Figure 5**a,b. Additionally, the calibration function of the cantilever specimen was compared with a known calibration function by Dowling,[27] showing negligible differences. Therefore, when proper values of $W$ or $W^*$ are used with presented calibration functions, the stress intensity factor values are not affected by the tapers introduced on the specimen (with relative difference of 7% at maximum for short cracks in PTP device and decreasing when the crack gets longer).

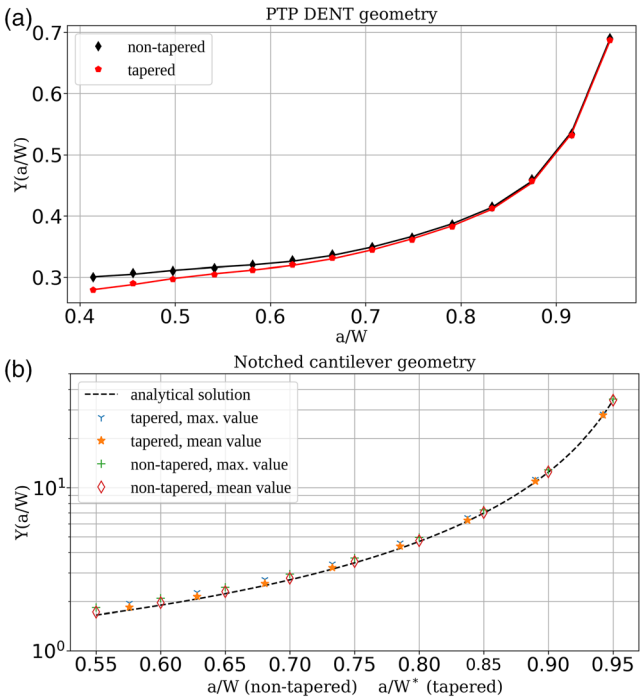


**Figure 5.** Plots of the evaluated calibration functions for tapered and non-tapered a) PTP device incorporating DENT specimen and b) notched cantilever specimens. In case of the cantilever, the lateral contraction of the free sides of the specimens caused a small crack portion affected by the mixed mode conditions, effectively decreasing the $K_I$ value. Therefore, two datasets are presented—one for $Y$-function evaluated for the maximum $K_I$ present at the crack front and the other one for the mean value of $K_I$ along the whole crack front, pushing the calibration function closer to the analytical solution which assumes pure plane strain mode I loading conditions.

As the FE analysis revealed, a tapered sample geometry can be employed to avoid printing artifacts and thereby increase the reliability of specimen fabrication to furthermore enhance the consistency within mechanical testing sets. **Figure 6**a provides original force versus displacement data (black dots) and the floating average filtered force signal (red line). In Figure 6b–d, in situ SEM images are depicted, corresponding to points marked via black arrows in Figure 6a. Here, Figure 6b was taken just before the crack initiation, Figure 6c just after and Figure 6d near the maximum displacement after considerable crack growth. Based on such in situ images, the overall crack length (secondary $y$-axis), including the notch, was determined at multiple points along the test and plotted in conjunction with the force versus displacement graph in Figure 6a. Utilizing this set of information, an elastic–plastic evaluation of the fracture process can be performed in the future.

To elucidate the deformation, and especially fracture behavior of the PTP devices with tension specimen geometry, also in situ SEM experiments were performed. The very first in situ testing observation revealed unintended deformation behavior in terms of an out of shape bending of the first design (see Figure 1b), which motivated the shape change toward thicker PTP arms. Further, the brittle and instable failure of the notched tension specimen was visually confirmed and backed via the force versus displacement data. As supervised experiments are more demanding, switching to the nonsupervised ex situ testing is desired once reproducible experiments are ensured and visual data are not required. In Figure 6e, ex situ testing data of a PTP device, as shown in Figure 3d, are depicted. The initial part of the trend shows the establishment of a contact between the indenter tip and the specimen top, followed by an increase in stiffness as the device is loaded. At a certain point, the specimen develops a plastic event at the notch, directly followed by unstable fracture, leading to a load drop. As the indentation is performed displacement controlled via a force-feedback loop, the abrupt load drops lead to an overshoot in displacement as testing artifact followed by a readjustment of the displacement as evident in the elastic unloading slope in Figure 6e. As the material fails spontaneously in tension at the loading, this artifact is negligible if considered correctly. For the evaluation of stable crack propagation, as shown for the cantilever specimen, an inherently displacement-controlled indenter is necessary to correctly track the force associated with crack extension at different speeds. After that, the displacement was still increased to a total displacement of about 3 µm before unloading. Figure 6f,g illustrate post-testing images of the device and a detailed view of the fractured specimen part. Figure 6h shows the postprocessing of the specific specimen to yield only the force versus displacement signal of the tension part. Therefore, a second loading cycle to a larger displacement of 4.5 µm is conducted following the first one. This enables a compliance correction of the PTP frame. Therefore, a cubic polynomial, where the constant is set to zero, is fitted to the second cycle's data to subsequently subtract the fit from the first loading cycle, under the assumption that the PTP frame deformed purely elastically during the first loading circle. This leaves the pure tension signal from the first loading cycle

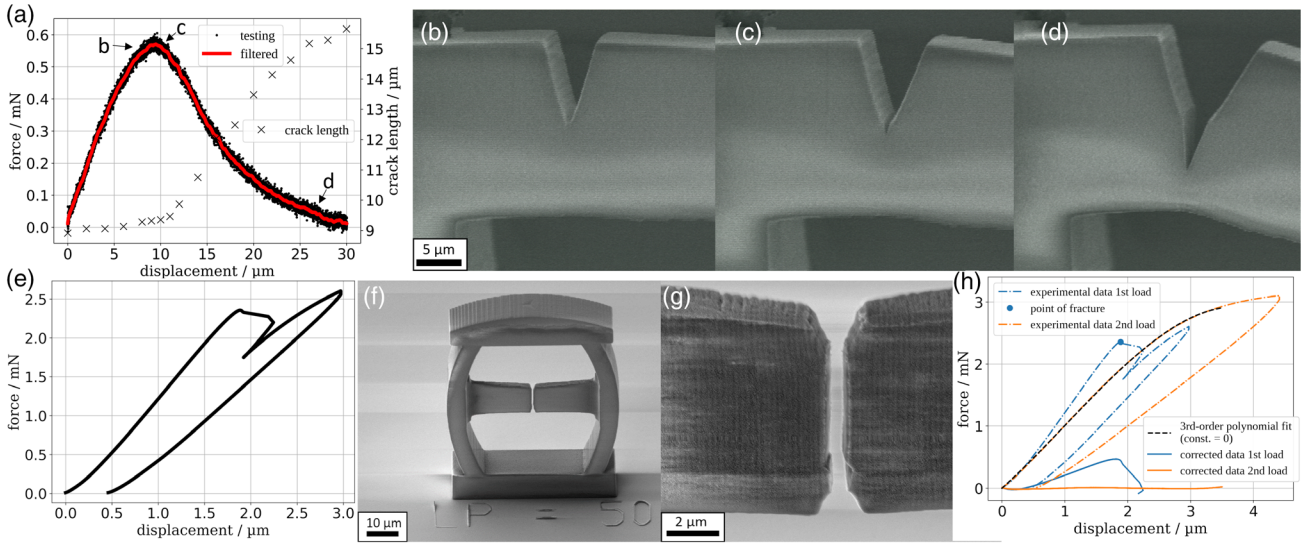


**Figure 6.** a) Representative force versus displacement data of an in situ fracture experiment on a notched cantilever along with correlated visually determined crack extension. b–d) SEM images during testing at stages indicated in (a), depicting the notched region (b) slightly before and (c) right after crack initiation as well as (d) after significant crack growth toward the maximum applied displacement. e) Ex situ experimental data of a PTP DENT geometry as indicated in Figure 3d. f) PTP geometry after testing and g) higher magnification on the notched specimen part, showing straight crack propagation with a slight deviation at the lower ligament region. h) Force versus displacement graph of the testing approach including second loading cycle and polynomial fit for the compliance correction of the PTP frame.

and the base line of the second loading, on which the accuracy of the fit is justified.

Following this data postprocessing, the fracture mechanical analysis is performed without a direct influence of the PTP frame. For a straightforward analysis, the point of maximum force is taken as conditional point of crack initiation, omitting small influences of viscoelasticity, plasticity, and potential stable crack growth just before unstable failure of the remaining specimen ligament. Via Equation (4) an energy-based $J$-integral evaluation is performed, where $U$ corresponds to the fracture energy as the integral of the force versus displacement signal until the maximum force was reached, $b_0 = W - a_0$, to the ligament as width minus both initial notch depth and $B$, the thickness of the specimen. The prefactor $\eta$ was set to 1 for a straightforward evaluation and to be compliant with pure energy approaches, not discriminating between elastic and plastic $J$ contribution with corresponding plastic work prefactor, which is somewhere between 0.8 and 1 for this sample shape.[28,29] Further small influences of asymmetry of both notches are omitted, indicated by Figure 4g.[26]

$$J_{IQ} = \frac{\eta * U}{b_0 * B} \tag{4}$$

A detailed evaluation of the materials fracture process according to a specific and suitable model is left for future studies.[30] Here, the focus is laid on the methodological approach to manufacture promising candidates for high-throughput testing approaches, facilitated by their straightforward testing procedure as, for example, via a common nanoindentation system. To demonstrate the presented approach nine specimen of equal geometry were printed, tested and evaluated in a high throughput manner. Together they show a $J_{IQ}$ of 100 J/m$^2$ with a standard deviation of 11 J/m$^2$. The criterion of $J_{IQ}/\sigma_0$, with yield strength $\sigma_0$ conservatively taken with 50 MPa from ref. [4], evaluates to 1.8 µm, which is explicitly larger than $B$, and therefore the crack initiation $J$-integral value is size-dependent, giving just a lower boundary for the materials inherent crack initiation toughness.

For comparison reasons, the fracture energy-based $J$-integral approach can be represented as stress intensity factor $K_{JIQ}$ via Equation (5), valid for plain stress condition and with $E$ being the Young's modulus of 3.2 GPa. The elastic modulus is chosen according to ref. [4], although similar but not exact equivalent writing parameters were employed for IP-DIP in this work.

$$K_{JIQ} = \sqrt{J_{IQ} * E} \tag{5}$$

With the estimation of Equation (4) the individual $J_{IQ}$ values were converted to $K_{JIQ}$, which yield a mean value of 0.57 MPam$^{1/2}$ with a standard deviation of 0.03 MPam$^{1/2}$. If this estimated value is compared to reported mode I fracture toughness values of chemically similar poly(methyl-methacrylate), which shows toughnesses in the range of 1 MPam$^{1/2}$ and well below, strongly dependent on the cross-linking density, a reasonably good agreement is present.[31] To further rationalize this estimation, a comparison with the FE simulation-based calibration of the structure is performed. Therefore, the linear elastic stress intensity factor $K_I$ at the point of fracture is estimated with Equation (1) and the geometry constant extracted from the $Y(a/W)$-graph at Figure 5a. The combined notch length, width, and thickness were used according to the printed specimen, where for $F$ a mean value over all nine fracture forces, meaning the directly accessible force on top of the

device before fracture along the first loading cycle according to the FE calibration model, is used. For this, a $K_I$ value at fracture of 0.38 $MPam^{1/2}$ is calculated, which is 33% lower than the result of the energy-based and converted $K_{JIQ}$, where $\eta$ was set to unity. The deviation presumably originates from applied simplifications and assumptions for the FE model in comparison to the real experiments, which can feature such as rounded edges of the actual geometry and the initial notch as well as small amounts of viscoelastic and/or plastic contributions, which are neglected by linear elastic considerations.

## 3. Conclusion and Outlook

This work illustrates how an elegant minor change in geometry, such as a 2° taper, can be applied on the digital model to avoid printing artifacts originating from drifting motion of initially printed layers, whereby the physical representation yielded about 4.4° for the case of the cantilever and 3.5° for the PTP specimen and might further vary slightly dependent on writing parameters and different geometries. By reducing the overhanging length between subsequently printed layers, stable and reproducible specimens are obtained, which is a prerequisite for reliable testing. Showcase load versus displacement graphs on optimized geometries are provided for in situ SEM mechanical testing on a miniaturized notched cantilever specimen and a PTP device incorporating a DENT specimen conducted ex situ in air. For the ex situ case, nine equivalent specimens were tested, which yielded a conditional crack initiation *J*-integral value of 100 $J/m^2$ with 11 $J/m^2$ standard deviation. Additionally, linear-elastic FE analyses were performed on real geometries to address the effect of the taper introduced at optimized geometries. Results show that no explicit side effect is detectable for the PTP DENT geometry, and just minor deviations due to the change of the ligament length in case of the notched cantilever geometry are present. Furthermore, both tapered and nontapered geometry functions were calculated for both specimen types. The introduced taper of the PTP DENT specimen resulted in a reduction of the geometry constant of about 6% at the presented printed specimens. From that, the linear elastic $K_I$ value for crack initiation is estimated 33% lower than the converted experimental values as from above, might be explained by the chosen simplifications and assumptions.

Both presented geometries are candidates for performing high-throughput mechanical testing on directly laser-written specimen. With the abbility to perform mechanical tests on direct laser written specimens, as demonstrated by the optimized PTP specimens, fundamental material properties and influences of various environmental conditionas as well as loading parameters can be determined with statistically backed data. However, it should be noted that also a wealth of further options arises. With just little alteration of the notch geometry, an assessment of the essential work of fracture[32] and similar experiments demanding a high number of specimens become feasible. For future experiments, similar geometries could be employed as universal test vehicles for coating materials.[1,2,25,33–35] Thereby, a wide combination of experiments emerges, reaching from a fast ex situ mechanical characterization over in situ SEM investigations to spatially resolved in situ synchrotron X-Ray diffraction experiments on identical specimen geometries. Thereby new experimental possibilities will enhance novel correlative material characterization and innovative material development approaches on a micrometer scale.

## 4. Experimental Section

*Design of the Notched Cantilever Specimen*: The geometries were designed with common aspect ratios in mind. For the notched cantilevers, a width ($W$) × thickness ($B$) × length ($L$) ratio of 1 × 1 × 5 was chosen, notched at 0.5 $W$ away from the pyramidal base and to half the thickness ($a_0/W = 0.5$). The base was designed to provide enough adhesion area and elevate the cantilever structure from the surface to enable testing via bending. To determine an optimized scaling of the specimens, different sizes were printed and tested in situ, where nominal dimensions of $20 \times 20 \times 100\,\mu m^3$ were found to give the best compromise in terms of response force, maximum available displacement, and printing time. In this case, printing without splitting to more than one print field was possible, leading to the fact that the overhanging features were always printed without interruption using constant printing parameters. At this point a detailed description of the physical geometry, after development of the specimen including shrinkage, as required for the fracture mechanical evaluation, is omitted.

*Design of the PTP Device Specimen*: For the rough shape of the PTP device, examples from the literature were employed, but completely redrawn to hold a DENT specimen.[25] The new design thereby aligns the tension specimen for in situ SEM tension experiments with perpendicular loading and imaging possibilities. The theoretical cross section of the tension specimen $W \times B$ is $12 \times 1\,\mu m^2$, with a double-sided notch $a_0$ of 3 µm each. As first experiments showed that the struts were insufficiently stiff (see Figure 1b,d), their thickness was increased considerably from 1.7 to 5.3 µm, except for previously discussed changes in the tension region. As tension loading is applied on the specimen, leading to roughly a squared correlation of reaction forces with size, the adjustment regarding the scaling of the geometry gives more freedom within constrains of the experimental setup. For this, the focus was laid on optimal printing time utilizing the highest precision and smallest specimen size, still resulting in a reasonably good tension specimen geometry and a minimum thickness of about 2 printing voxel diameters. The actual dimensions of the tension specimen after printing were for the width at specimen base, excluding the tapered region, $W = 12.6\,\mu m$, the thickness $B = 0.6\,\mu m$, the combined initial notch depths $a_0 = 5.7\,\mu m$ giving an initial ligament $b_0 = W - a_0 = 6.9\,\mu m$.

*Direct laser Writing of Specimen*: The geometry files were constructed via FreeCAD (Version: 0.18.) and exported as stl format to perform direct laser writing by two-photon lithography via the available device (Photonic Professional GT2, NanoScribe GmbH & Co. KG, Eggstein-Leopoldshafen, Germany). The standard procedure for small features was used, including 1"×1" fused-silica substrates, a 63× Objective (Plan-APOCHROMAT 63 × N.A. 1.4 Oil DIC, Carl Zeiss AG, Oberkochen, Germany), and IP-DIP (Nanoscribe GmbH & Co. KG, Eggstein-Leopoldshafen, Germany) as photo resin. Slicing of the models was performed with 100 nm distance, a hatching distance of 200 nm, and a shift of line direction by 90° between each layer. The printing was performed with 10 $\mu m\,s^{-1}$ writing speed and 20 mW laser power, with exception of the optimized PTP geometry, where it was slightly increased to 25 mW. To fit printed parts within the in situ SEM testing setup, the fused silica substrate was prepared previously to printing. First, grooves were introduced via a diamond wire saw (type: 6234, well Diamantdrahtsägen GmbH, Mannheim, Germany) in a square fashion giving about 5 × 5 mm partitions, along the edges of which specimens were printed at a distance of a few 10 µm. After printing a standard development procedure, including 20 min submersion in propylene-glycol-methyl-ether-acetate and 5 min isopropyl alcohol, was applied, followed by a gold coating via a sputter coating machine (Sputter Coater 108auto, Cressington Scientific Instruments Ltd., Watford, UK) to enhance surface conductivity

and improve SEM imaging. A ceramic scriber was employed to introduce precracks followed by manual partitioning of the substrate and mounting for the in situ experiments. In case of the in situ experiments on the PTP devices, the same procedure was used, while for the ex situ case no pre-preparation was done, but gold coating was applied equally to enhance later SEM investigations.

*SEM Imaging and Mechanical Experiments*: The in situ mechanical experiments were performed via a nanoindenter system (UNAT-SEM 1, ASMEC GmbH, Dresden, Germany) within an SEM (LEO 982, Carl Zeiss GmbH, Oberkochen, Germany). The bending experiments were performed by loading the cantilever at about 60 µm from the notch through a wedge-shaped indenter (Synton MDP, Nidau, Switzerland) displacement controlled to a maximum displacement of 30 µm with 100 nm $s^{-1}$ loading rate and 33 Hz force acquisition rate. Each second two SEM images (acceleration voltage: 1 kV) were recorded, enabling to determine the crack extension afterward. To reduce testing noise in the force signal, a moving average filter, as convolution over 100 nearest data points, was applied.

For the ex situ experiment in air, a force controlled nanoindenter (TS 77 Triboindenter, Hysitron Inc., Eden Prairie, USA) was employed, to load the PTP device via a Berkovich indenter tip, with a displacement rate of 100 nm $s^{-1}$, through a feedback loop. The force acquisition rate was 100 Hz. All images, except from the in situ experiment, were acquired with another SEM (AURIGA, Carl Zeiss AG, Oberkochen, Germany), but also using 1 kV acceleration voltage.

*Finite Element Simulation*: To accurately transfer the cantilever and PTP specimens into the numerical model, original 3D geometry files (previously used for the 3D printing) were utilized. For the adjustments of the original geometry and numerical FE modeling, the Abaqus/CAE 2019 software (Dassault Systèmes Simulia Corp., Vélizy-Villacoublay, France) has been employed.

The cantilever beam was modeled as a full 3D model including the base of the device (**Figure 7**). A rectangular cross section of the nontapered cantilever beam was assumed to be 20 × 20 µm and a sharp V-notch with depth of 10 µm was modeled at the distance of 60 µm from the loading line. By cutting off the 4.4° taper at the bottom side of the cantilever, the tapered specimen model was created (Figure 7a). As a loading, the line-force load was applied to produce a maximal total load of 1 mN in the direction perpendicular to the main cantilever axis (Figure 7b). The bottom face of the base of the model was fixed (assuming zero displacements in all directions) to model the real specimen displacement.

The PTP device geometry (**Figure 8**) was simplified using two symmetry planes, allowing efficient and fast modeling of its complex 3D geometry. With the use of the symmetry, only one quarter of the whole specimen had to be modeled, using appropriate symmetrical boundary conditions (fixed displacement in the direction perpendicular to the symmetry plane). On the bottom of the PTP device, the fixed boundary condition was applied. The loading in the FE model was created using a rigid plate compressing the PTP device via a frictionless contact. With the use of this type of loading, the experimental loading using a blunt indenter tip to push down the device from the top was accurately modeled. The total loading force applied on the rigid plate in the one-quarter model was 0.5 mN, therefore equivalent to 2 mN when applying the force on the full model. Furthermore, an additional model for the geometry calibration of the specimen was created in case of the PTP device. To use more efficient modeling, only a half of the original model was used, as shown in Figure 8c, where an additional symmetry plane was introduced. While this simplification ignores any possibility of the whole central portion of the specimen to bend, it avoids introduction of nonsymmetrical crack propagation, making the direct comparison between the tapered and nontapered geometry more straightforward. As the introduction of a taper is symmetrical, there

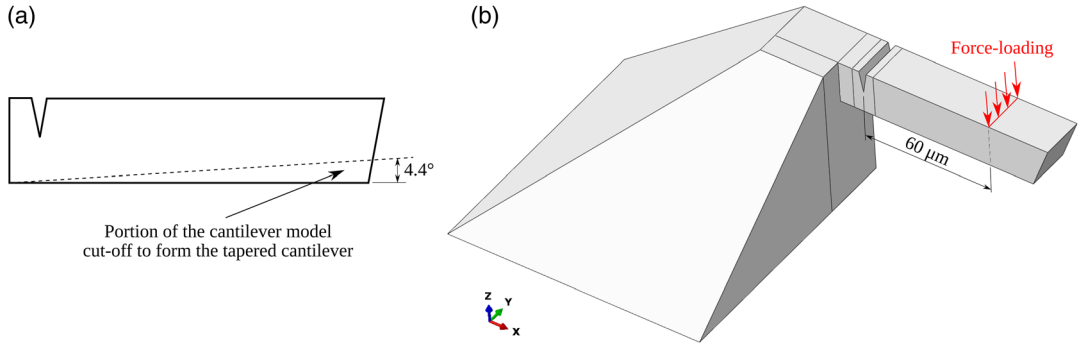


**Figure 7.** Model of the cantilever specimen: a) scheme of the difference between the tapered and nontapered geometry (side view on the cantilever beam). b) Geometry used for the FE model (nontapered cantilever) with depicted loading.

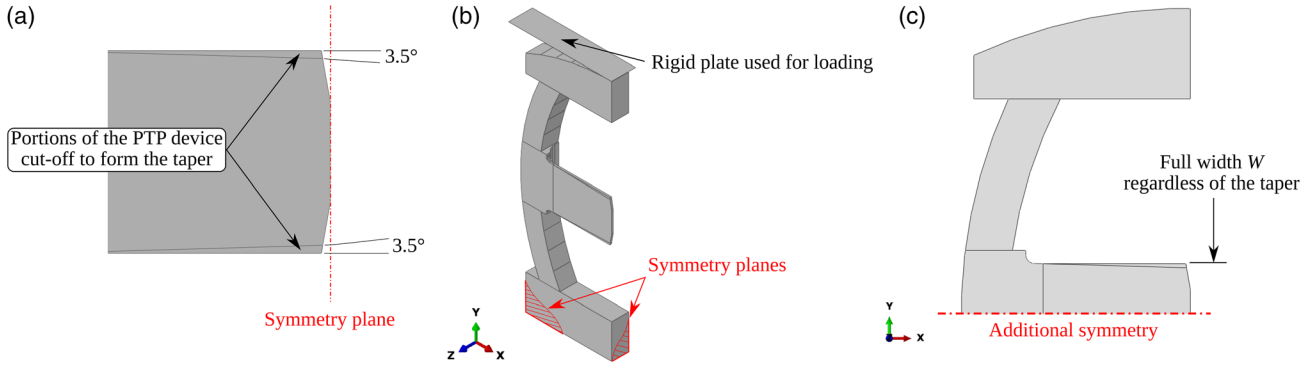


**Figure 8.** Model of the PTP specimen: a) scheme of the difference between tapered and nontapered geometry (detail on the central portion of the notched part of the model, side view); b) geometry used for the FE model (nontapered PTP device) with the rigid plate used for loading; c) geometry of the model used for the calibration function *Y*.

is no impact on the crack propagation direction or starting point, and therefore the use of additional symmetry is justified.

In both FE models, a purely elastic material model was used as approximation of the real material mechanical behavior. The Young's modulus was set to 3.2 GPa and the Poisson's ratio was set to 0.4 (usual value used for polymeric materials).[4] For the FE mesh discretization, full 3D linear and quadratic elements (C3D8R and C3D20R) were used with the finer mesh at the area of interest in vicinity of the notch. The mesh was checked for three different configurations (element sizes and nodes configuration) in relation to changes to the evaluated *K*-values leading to slightly underestimated values for a very rough mesh, but no changes between the two finer discretization types. Therefore, the finest mesh was used and deemed appropriate in terms of this analysis (furthermore solidified with the good agreement between the analytical and FE solution, see Results section). As results, the loading force–displacement relation at the place of loading was extracted as well as the stress and strain fields in the bulk of the models.

## Acknowledgements

Financial support by Montanuniversität Leoben and the European Research Council for the ERC project TOUGHIT (project number 771146) is gratefully acknowledged.

## Conflict of Interest

The authors declare no conflict of interest.

## Data Availability Statement

The data that support the findings of this study are available from the corresponding author upon reasonable request.

## Keywords

finite element modeling, micromechanics, notched cantilever, push-to-pull devices, two-photon lithography

Received: February 28, 2022
Revised: May 13, 2022
Published online: June 5, 2022

[1] L. R. Meza, A. J. Zelhofer, N. Clarke, A. J. Mateos, D. M. Kochmann, J. R. Greer, *Proc. Natl. Acad. Sci. U.S.A.* **2015**, *112*, 11502.
[2] A. Schroer, J. M. Wheeler, R. Schwaiger, *J. Mater. Res.* **2018**, *33*, 274.
[3] E. D. Lemma, F. Rizzi, T. Dattoma, B. Spagnolo, L. Sileo, A. Qualtieri, M. De Vittorio, F. Pisanello, *IEEE Trans. Nanotechnol.* **2016**, *16*, 23.
[4] N. Rohbeck, R. Ramachandramoorthy, D. Casari, P. Schürch, T. E. J. Edwards, L. Schilinsky, L. Philippe, J. Schwiedrzik, J. Michler, *Mater. Des.* **2020**, *195*, 108977.
[5] J. Purtov, A. Verch, P. Rogin, R. Hensel, *Microelectron. Eng.* **2018**, *194*, 45.
[6] J. Bauer, A. G. Izard, Y. Zhang, T. Baldacchini, T. Baldacchini, L. Valdevit, L. Valdevit, *Opt. Express* **2020**, *28*, 20362.
[7] J. S. Oakdale, J. Ye, W. L. Smith, J. Biener, *Opt. Express* **2016**, *24*, 27077.
[8] J. Bauer, A. Schroer, R. Schwaiger, O. Kraft, *Nat. Mater.* **2016**, *15*, 438.
[9] A. Albiez, R. Schwaiger, *MRS Adv.* **2019**, *4*, 133.
[10] A. Zakhurdaeva, P.-I. Dietrich, H. Hölscher, C. Koos, J. G. Korvink, S. Sharma, *Micromachines* **2017**, *8*, 285.
[11] G. Seniutinas, A. Weber, C. Padeste, I. Sakellari, M. Farsari, C. David, *Microelectron. Eng.* **2018**, *191*, 25.
[12] A. A. Bauhofer, S. Krödel, J. Rys, O. R. Bilal, A. Constantinescu, C. Daraio, *Adv. Mater.* **2017**, *29*, 1703024.
[13] J. Li, S. Thiele, B. C. Quirk, R. W. Kirk, J. W. Verjans, E. Akers, C. A. Bursill, S. J. Nicholls, A. M. Herkommer, H. Giessen, R. A. McLaughlin, *Light: Sci. Appl.* **2020**, *9*, 124.
[14] P.-A. Blanche, M. Neifeld, N. Peyghambarian, *Sci. Rep.* **2017**, *7*, 17767.
[15] S. Coelho, J. Baek, J. Walsh, J. Justin Gooding, K. Gaus, *Nat. Commun.* **2022**, *13*, 647.
[16] K. T. P. Lim, H. Liu, Y. Liu, J. K. W. Yang, *Nat. Commun.* **2019**, *10*, 25.
[17] M. Blaicher, M. R. Billah, J. Kemal, T. Hoose, P. Marin-Palomo, A. Hofmann, Y. Kutuvantavida, C. Kieninger, P.-I. Dietrich, M. Lauermann, S. Wolf, U. Troppenz, M. Moehrle, F. Merget, S. Skacel, J. Witzens, S. Randel, W. Freude, C. Koos, *Light: Sci. Appl.* **2020**, *9*, 71.
[18] A. Erben, M. Hörning, B. Hartmann, T. Becke, S. A. Eisler, A. Southan, S. Cranz, O. Hayden, N. Kneidinger, M. Königshoff, M. Lindner, G. E. M. Tovar, G. Burgstaller, H. Clausen-Schaumann, S. Sudhop, M. Heymann, *Adv. Healthcare Mater.* **2020**, *9*, 2000918.
[19] R. K. Jayne, M. Ç. Karakan, K. Zhang, N. Pierce, C. Michas, D. J. Bishop, C. S. Chen, K. L. Ekinci, A. E. White, *Lab Chip* **2021**, *21*, 1724.
[20] M. Kaynak, P. Dirix, M. S. Sakar, *Adv. Sci.* **2020**, *7*, 2001120.
[21] J. Knoška, L. Adriano, S. Awel, K. R. Beyerlein, O. Yefanov, D. Oberthuer, G. E. P. Murillo, N. Roth, I. Sarrou, P. Villanueva-Perez, M. O. Wiedorn, F. Wilde, S. Bajt, H. N. Chapman, M. Heymann, *Nat. Commun.* **2020**, *11*, 657.
[22] C. C. J. Alcântara, F. C. Landers, S. Kim, C. D. Marco, D. Ahmed, B. J. Nelson, S. Pané, *Nat. Commun.* **2020**, *11*, 5957.
[23] R. K. Jayne, T. J. Stark, J. B. Reeves, D. J. Bishop, A. E. White, *Adv. Mater. Technol.* **2018**, *3*, 1700293.
[24] M. Schmid, D. Ludescher, H. Giessen, *Opt. Mater. Express* **2019**, *9*, 4564.
[25] J. Bauer, A. Schroer, R. Schwaiger, I. Tesari, C. Lange, L. Valdevit, O. Kraft, *E.M.L.* **2015**, *3*, 105.
[26] T. L. Anderson, *Fracture Mechanics: Fundamentals and Applications*, 3th ed., CRC Press, Boca Raton, FL, USA **2004**.
[27] N. E. Dowling, *Mechanical Behavior of Materials*, 4th ed., Pearson, London, England, GB **2012**
[28] J. Zechner, M. Janko, O. Kolednik, *Compos. Sci. Technol.* **2013**, *74*, 43.
[29] C. D. Wilson, P. Mani, *Eng. Fract. Mech.* **2008**, *5*, 5177.
[30] M. Elices, G. V. Guinea, J. Gómez, J. Planas, *Eng. Fract. Mech.* **2002**, *69*, 137.
[31] D. C. Miller, S. R. Kurtz, *Sol. Energy Mater. Sol. Cells* **2011**, *95*, 2037.
[32] A. B. Martinez, J. Gamez-Perez, M. Sanchez-Soto, J. I. Velasco, O. O. Santana, M. L. Maspoch, *Eng. Failure Anal.* **2009**, *16*, 2604.
[33] E. Almog, A. Sharma, Y. Qi, J. Zimmerman, E. Rabkin, *Acta Mater.* **2022**, *225*, 117552.
[34] T. Juarez, A. Schroer, R. Schwaiger, A. M. Hodge, *Mater. Des* **2018**, *140*, 442.
[35] R. Malureanu, M. Zalkovskij, A. Andryieuski, A. V. Lavrinenko, *J. Electrochem. Soc.* **2010**, *157*, K284.